Ultrafast doublon dynamics in photo-excited $1T$-TaS_2 - Supplementary material

M. Ligges[1],* I. Avigo[1], D. Golež[2], H. U. R. Strand[2], Y. Beyazit[1], K. Hanff[3], F. Diekmann[3], L. Stojchevska[1], M. Kalläne[3], P. Zhou[1], K. Rossnagel[3], M. Eckstein[4], P. Werner[2], and U. Bovensiepen[1]
[1]*Faculty of Physics, University of Duisburg-Essen, 47048 Duisburg, Germany*
[2]*Department of Physics, University of Fribourg, 1700 Fribourg, Switzerland*
[3]*Institute of Experimental and Applied Physics, University of Kiel, 24098 Kiel, Germany and*
[4]*Max Planck Research Department for Structural Dynamics, University of Hamburg-CFEL, 22761 Hamburg, Germany*
(Dated: December 28, 2017)

SAMPLE GROWTH AND CHARACTERIZATION

Single crystals of $1T$-TaS_2 were grown by the standard chemical vapor transport method: A near-stoichiometric mixture of high-purity Ta and S with a slight S excess (1 mg/cm^3) was placed in a quartz ampoule together with iodine (5-8 mg/cm^3) as transport agent; the ampoule was sealed and heated in a four-zone furnace under a temperature gradient. Two different growth conditions were chosen. Samples of batch No. 1141R (as discussed in the manuscript) were grown in a temperature gradient of 960-860 °C within 600 h, and for samples of batch No. 1206R an identical growth cycle was followed by additional 150 h of heating in a gradient of 990-980 °C. In both cases, the formation of polytypes other than the $1T$ type was prevented by quenching of the hot ampoules in water. Typical crystal sizes were about 5×5×0.1 mm^3.

Compared to other transition-metal dichalcogenides, $1T$-TaS_2 crystals tend to exhibit higher defect concentrations and stronger sample dependence of the low-temperature properties. This is likely due to the quenching process. Figure 1a shows temperature-dependent resistance curves characteristic for samples from the two batches grown under the conditions mentioned above. These data serve to indicate sample variability in the present study, and we note that they are remarkably similar to the curves presented in Fig. 1 of Ref. [1], where similar growth temperatures were used.

Despite similar growth conditions, both sample batches show significantly different behavior in both, electrical resistance and time-resolved photoemission (Fig. 1b.) The resistance curve of the sample from batch No. 1206R displays a narrower hysteresis of the nearly commensurate-to-commensurate charge-density-wave (CDW) transition around 200 K as well as a more pronounced resistance increase at low temperatures. These signatures are commonly associated with a higher concentration of defects, a stronger tendency toward Anderson localization, and thus a lower carrier concentration at low temperatures in the commensurate CDW phase [1]. For these samples, only a vague signature of the UHB was observed in the femtosecond photoemission spectrum (Fig. 1b.).

A reliable quantitative determination of the carrier concentration or doping level in $1T$-TaS_2 samples is a formidable task beyond the scope of the present study. However, a case can be made here for hole-type doping. Samples with resistivity curves similar to the ones depicted in Fig. 1a have been shown to be Ta deficient, i.e., the corresponding (thermodynamically most stable) compounds are rather described as $1T$-$Ta_{1-x}S_2$ with x≤0.03 [2][3]. In a simple ionic bonding model, each missing Ta ion would donate 4 holes to the system so that a cluster of 13 Ta atoms would be doped by ≤1.6 holes. This value, however, should be regarded as an upper limit because bonding in transition-metal dichalcogenides is not purely ionic and because the value would correspond to a complete emptying of the sub-band at E_F and thus a suppression of the Mott transition, which is not observed. Measurements of the Hall coefficient provide further evidence for hole doping, though at much lower levels. For samples with resistivity curves similar to the ones shown in Fig. 1a, positive Hall coefficients are consistently found for the commensurate CDW phase, indicating p-type conductivity. At a temperature of about 30 K, the extracted hole densities are in the range of 0.03-0.12% per Ta atom or 0.4-1.6% per 13-Ta-atom cluster, assuming a one-carrier

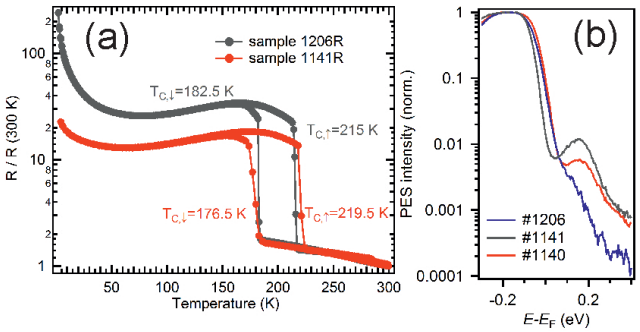

FIG. 1. (color). Comparsion of two different growth batches 1141R (as discussed throughout the manuscript) and 1206R. (a) Normalized resistance as a function of temperature upon heating and cooling for two samples from different batches. Indicated transition temperatures represent midpoints of the resistance jumps. (b) Corresponding time-averaged (Δt=-95..-35 fs) photoemission spectra obtained from both samples. The data was recorded at T=80 K with F=50-60 μJ/cm^2. A third trace obtained from sample ♯1140 is also shown.

model [1, 4].

As a final, independent piece of evidence for finite hole doping levels, we present in Fig. 2 soft x-ray ARPES Fermi surface data as obtained from a sample of batch No. 1141R. While the ARPES Fermi surface can in

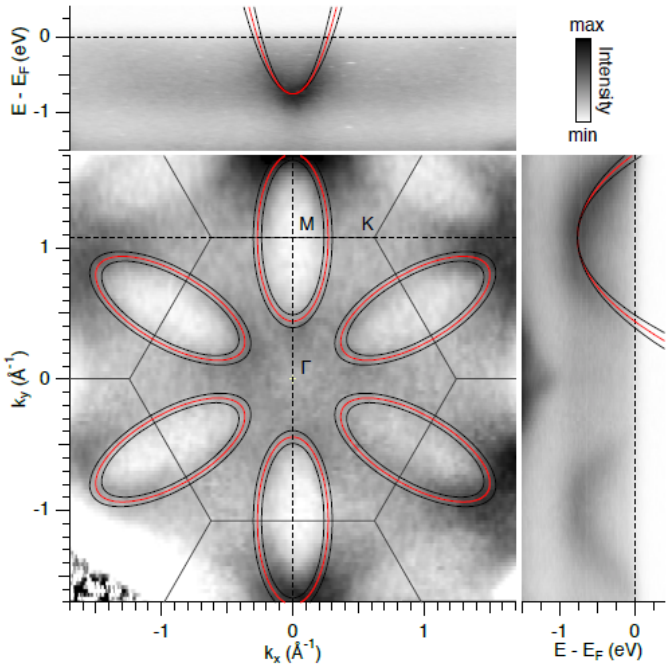

FIG. 2. (color). ARPES intensity distributions taken from a $1T$-TaS_2 sample of batch No. 1141R at $T = 390$ K (hν=270 eV). Middle: Self-normalized E_F-intensity map covering the first (hexagonal) Brillouin zone. Top and right: E-versus-k maps of the original photoemission intensity along the high-symmetry paths indicated by the dashed lines in the middle panel. Solid red curves represent extracted elliptical Fermi contours (middle) and parabolic band dispersions (top and right), respectively. Solid black curves indicate the uncertainty in the analysis. The ARPES data were measured at beamline P04 (end station ASPHEREIII) of PETRA III at DESY.

principle be a direct measure for the band filling, the analysis is often complicated by matrix-element effects, and it is not at all straightforward in the case of $1T$-TaS_2. First, the measured bands are unusually broad even at low temperatures. Second, the Fermi surface is completely gapped in the low-temperature commensurate CDW phase and it remains partially gapped or pseudogapped up to temperatures significantly above room temperature. The data shown here were measured at a temperature of 390 K with a photon energy of 270 eV, for which the $k_\perp$ component of the photoelectron wavevector is close to a Γ-M-K plane. The central panel of Fig. 2 shows the $k_\parallel$-dependent photoemission intensity distribution from the Fermi edge divided at each $k_\parallel$ point by the energy-integrated Ta $5d$ intensity of the underlying energy distribution curve. This "self-normalization" is a common and robust method to reduce the influence of the $k_\parallel$-dependent photoemission matrix element [5]. The side panels show the original $E(k_\parallel)$ intensity distributions along the M-Γ (right) and M-K (top) high-symmetry directions, respectively.

From this data set, the volume of the Fermi surface was estimated as follows. The electron-like Fermi surface pockets centered on the M points were approximated as ellipses. The underlying two-dimensional parabolic band dispersion was defined by three characteristic $(E, k_\parallel)$ points that were only weakly affected by the spectral weight changes due to CDW gap or pseudogap formation near E_F: the bottom of the band at M and the band positions at 0.4 eV below E_F along the M-Γ and M-K line, respectively. These three points were determined for each of the six ellipses from second-gradient E-versus-k maps along the respective high-symmetry directions. The Fermi vectors resulting from the approximated band dispersion are $k_{xF} = (0.270\pm0.032)$ Å^{-1} (M-K direction, semiminor axis) and $k_{yF} = (0.637\pm0.049)$ Å^{-1} (M-Γ direction, semimajor axis). The corresponding Fermi ellipses and band dispersions including minimum and maximum deviations are indicated in Fig. 2. Dividing the total area of six ellipses by the area of the surface projected Brillouin zone finally gives the Ta $5d$ band filling: (0.81±0.16) electrons per Ta atom, assuming a lattice constant of 3.365 Å [6]. We note that the analysis is afflicted with a large uncertainty and that the average value is unrealistically low, but that near-stoichiometric band fillings are within the error bars and that there appears to be a clear tendency toward less than half filling.

PUMP WAVELENGTH DEPENDENCE

As described in the main text, the pump photon energy of 1.55 eV largely exceeds the energetic separation of the LHB and UHB spectral signature of approximately 350 meV, raising questions on the underlying excitation mechanism for the population of the UHB. We performed additional experiments using infrared pump pulses provided by an optical parametric amplifier. Time-averaged spectra obtained from these measurements are shown in Fig. 3 in direct comparsion to corresponding reference measurements performed with 1.55 eV pump photon energy on the same samples. At both other pump photon energies used, the UHB signature is absent. This finding supports the suggested excitation scheme mentioned in the main manuscript, where the UHB signature is populated by resonant excitation from a lower lying band at $E - E_F \approx -1.3$ eV [7, 8], while the LHB signature is simultaneously depopulated by excitation to higher energies. It should be stressed that resonant population of the UHB should be possible from other occupied bands, as recently shown by Carbone and coworkers [9] and, thus, the appearance of the signature should not be tied to

excitation with 1.55 eV energy photons.

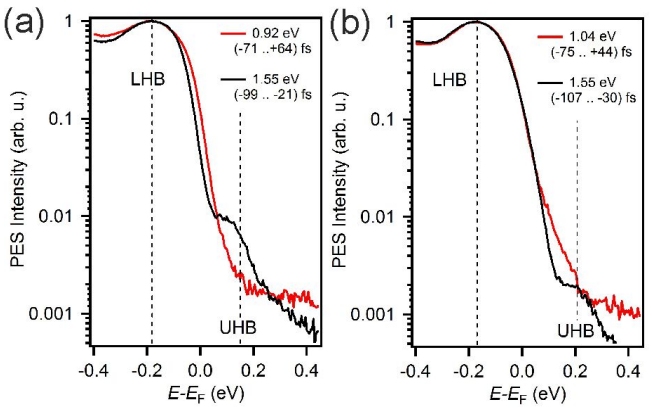

FIG. 3. (color). Comparsion of time-averaged spectra obtained with (a) 0.92 eV and (b) 1.04 eV pump photon energy. The corresponding reference measurements with 1.55 eV pump photons are shown for direct comparsion. Measurements were performed at T=80 K with excitation fluences F=50 μJ/cm^2.

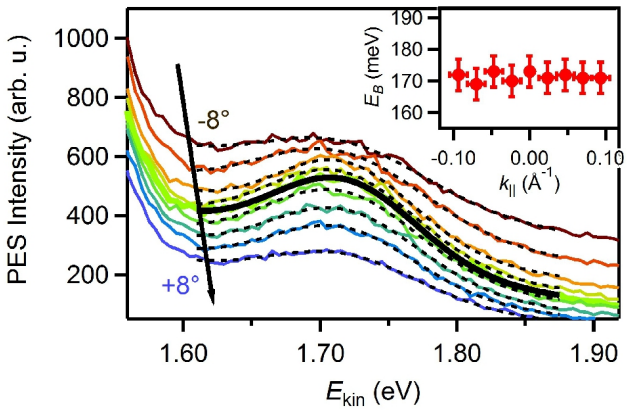

FIG. 4. (color). Energy distribution curves at Δt = 0 for different emission angles. Dashed lines represent fits to the data. The solid line indicates the spectrum recorded in normal emission. The extracted dispersion of the UHB is shown in the inset, where E_B denotes the energy of the UHB with respect to the Fermi level.

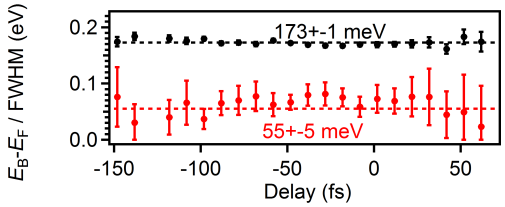

FIG. 5. (color). UHB energy $E_{\rm B}$ (referenced to Fermi level $E_{\rm F}$) and spectral width (full width at half maximum) as a function of delay for the data shown in the main text (black and red points, respectively). The dashed lines are error-weighted constant fits.

SPECTRAL PROPERTIES OF THE UHB

The dispersion of the UHB was analyzed by tilting the orientation of the sample with respect to the spectrometer entrance. Due to the low kinetic energy of the emitted electrons and the limited tilting angle, only a small region of $k_{||}$ around the zone center was accessible. Fig. 4 shows energy distribution curves recorded for different emission angles at a fixed delay time, where the spectroscopic contrast was highest (Δt = 0). The data was recorded at T = 30 K and F=110 $\mu J/cm^2$.

The energy distribution curves were fitted as described in the main text and the results are shown in the inset of Fig. 4. No significant dispersion of the UHB is observed. This matches the expectations from the simple Hubbard model, where the dispersion of the LHB and UHB and the corresponding bandwidth are similar.

We furthermore analyzed the temporal evolution of the UHB spectral width and peak position as a function of delay time by fitting the individual spectra as explained in the main text. Fig. 5 shows both quantitites as a function of delay time for the data presented in the manuscript (T=30 K, F=60 μJ/cm^2). Within the experimental accuracy, no changes in the UHB peak position or width could be identified, which indicates a rapid thermalization of doublons that can not be resolved in our experiments.

DOUBLON LIFE TIME ESTIMATION

The data discussed throughout the manuscript is mainly that obtained for low temperatures (T=30 K) and under weak excitation conditions (F=60 $\mu J/cm^2$). The corresponding time-dependent UHB intensities are shown in Fig. 6a, including error bars obtained from the individual fits to the transient energy distribution curves.

Under these excitation conditions, the population dynamics can be analyzed in detail, resulting in the statement in the main manuscript that the doublon dynamics were estimated to occur on a time scale faster than or equal to 20 fs. Such characteristic life times can be extracted by analyzing potential temporal asymmetries in the population dynamics. In Fig. 4a, error-weighted Gaussian fits to the population dynamics are shown with limits ranging from large negative to finite positive and finite negative to large positive delays (blue and black curve, respectively). Both fits essentially give the same result with only minor variations that result in an overall error of approximately 20 fs, as stated in the main

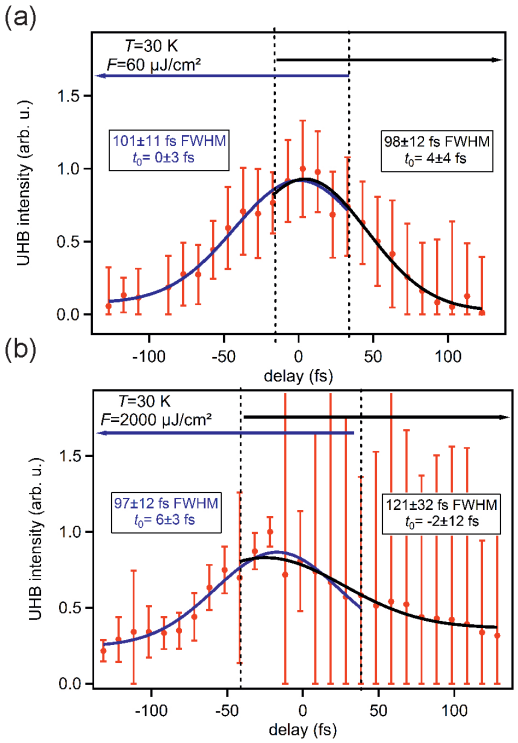

FIG. 6. (color). Population dynamics of the UHB in the weak (a) and strong (b) excitation limit (F=60 $\mu J/cm^2$ and F=2000 $\mu J/cm^2$, respectively). The data was fitted with Gaussian functions (error weighted), taking into account the left hand data or the right hand data (blue and black solid lines).

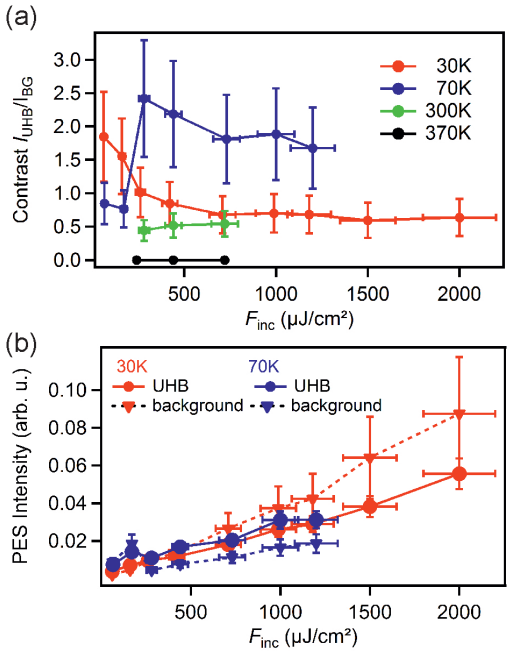

FIG. 7. (color). (a) Spectroscopic contrast $I_{\mathrm{UHB}}/I_{\mathrm{BG}}$ of the UHB with respect to the underlying background for different sample base temperatures as a function of incident fluence. (b) Intensity of the UHB and the background for T=30 K and T=70 K as a function of incident fluence.

manuscript. Similar analysis of data obtained at higher excitation fluences yielded in principle the same result, however, with larger errors. As an extreme example, the data and corresponding fits for the measurements performed with $F = 2000\ \mu J/cm$ are shown in Fig. 6b, where no statistically relevant values can be extracted. In particular the error bars at positive delays increase significantly due to an enhanced build-up of secondary excitations, which mask the spectral signature of the UHB.

SPECTROSCOPIC CONTRAST AND TEMPERATURE DEPENDENCE

Experiments at fixed delays were performed to analyze the spectroscopic contrast $I_{\mathrm{UHB}}/I_{\mathrm{BG}}$ of the UHB with respect to the underlying incoherent excitation continuum for different temperatures and different excitation strength. The results are shown in Fig. 7a. While in general the contrast decreases with increasing temperature and excitation fluence, the highest contrast was obtained at a base temperature of 70 K. Considering the co-existance of metallic and insulating domains at elevated temperatures of $1T$-TaS_2, one would expect that the UHB intensity constantly decreases as a function of sample temperature, as the amount of insulating domains within the probed sample area gradually decreases. In fact, we find that under similar experimental conditions, the UHB intensity is approximately the same for T=30 K and T=70 K (Fig. 7b). However, the underlying background is roughly 50% higher at lower base temperature, resulting in an lower effective spectroscopic contrast. The underlying dynamics that result in the build-up of the incoherent background can be complex and are directly linked to, e.g., the transient gap size, effective free carrier density and available phase space for secondary excitations. We stress that also the optical properties of $1T$-TaS_2 are strongly temperature-dependent [10] and might furthermore underly transient changes upon pumping, resulting in effectively higher or lower absorbed excitation fluence. In order to reduce the influence of thermal fluctuations and phonons on the UHB dynamics, we thus performed our main measurements at the lowest possible base temperature of T=30 K.

* manuel.ligges@uni-due.de

[1] R. Inada, Y. Onuki, and S. Tanuma, J. Phys. Soc. Jpn. **52**, 3536 (1983).
[2] T. Endo, S. Nakao, W. Yamaguchi, T. Hasegawa, and K. Kitazawa, Solid State Commun. **116**, 47 (2000).
[3] In the Supp. Mat. of [11], a convincing SEM/EDX analysis of the chemical composition is presented, with x=

0.026.
[4] R. Inada, Y. Onuki, and S. Tanuma, Phys. Lett. A **69**, 453 (1979).
[5] S. V. Borisenko, A. Kordyuk, S. Legner, C. Dürr, M. Knupfer, M. Golden, J. Fink, K. Nenkov, D. Eckert, G. Yang, S. Abell, H. Berger, L. Forró, B. Liang, A. Maljuk, C. Lin, and B. Keimer, Phys. Rev. B **64**, 094513 (2011).
[6] K. Rossnagel, J. Phys.: Condens. Matter **23**, 213001 (2011).
[7] N. Smith, S. Kevan, and F. DiSalvo, J. Phys. C: Solid State Phys. **18**, 3175 (1985).
[8] M. Arita, H. Negishi, K. Shimada, F. Xu, A. Ino, Y. Takeda, K. Yamazako, A. Kimuar, S. Qiao, S. Negishi, M. Sasaki, H. Namatame, and M. Taniguchi, Physica B **351**, 265 (2004).
[9] A. Mann, E. Baldini, A. Odeh, A. Magrez, H. Berger, and F. Carbone, Phys. Rev. B **94**, 115122 (2016).
[10] A. R. Beal, H. P. Hughes, and W. Liang, J. Phys. C **8**, 4236 (1975).
[11] A. Ribak, I. Silber, C. Baines, K. Chashka, Z. Salman, Y. Dagan, and A. Kanigel, Phys. Rev. B **96**, 195131 (2017).